Clays and Clay Minerals, Vol. 59, No. 5, 490–500, 2011.

A CRITICAL TEXTURAL EVOLUTION STUDY OF ZEROVALENT IRON/MONTMORILLONITE NANOSIZED HETEROSTRUCTURES UNDER VARIOUS IRON LOADINGS

MINGDE FAN[1,2], PENG YUAN[2,*], FAÏZA BERGAYA[3], HONGPING HE[2], TIANHU CHEN[4], JIANXI ZHU[2], AND DONG LIU[2,5]

[1] College of Environment and Resources, Inner Mongolia University, Hohhot 010021, China
[2] CAS Key Laboratory of Mineralogy and Metallogeny, Guangzhou Institute of Geochemistry, Chinese Academy of Sciences, Guangzhou 510460, China
[3] CRMD CNRS-Université d'Orléans, 1b, Rue de la Férollerie, 45071 Orléans Cedex 2, France
[4] School of Resources and Environmental Engineering, Hefei University of Technology, Hefei 230009, China
[5] Graduate School of the Chinese Academy of Science, Beijing 100039, China

Abstract—Heterostructures formed by nanoparticles hybridized with porous hosts are of great potential in many practical applications such as catalysis, adsorption, and environmental remediation, based on their intrinsic properties. The objectives of this study were to synthesize zerovalent iron nanoparticles/montmorillonite heterostructures and to investigate their textural evolution under different Fe loadings. Iron nanoparticles were hybridized with montmorillonite by impregnation of montmorillonite by ferric ions followed by chemical reduction with sodium borohydride in solution. These hybridized Fe nanoparticles were well dispersed on the montmorillonite surface, size adjustable, and resistant to oxidation under the protection of native Fe-oxide shells. The textural evolution of these heterostructures under various Fe loadings was investigated using nitrogen physisorption, X-ray diffraction, electron microscopy, and elemental analyses. As the Fe loadings increased, the total pore and mesopore volumes were almost unchanged; the total, micropore, and external surface areas as well as the micropore volume decreased; and the average pore diameter increased. These textural changes could be attributed to the filling of the interparticle pores of montmorillonite by a variable amount of Fe nanoparticles. In addition, with increasing Fe loadings, the mesoporous character was enhanced for these heterostructures. These fundamental results are important in understanding the structure of these heterostructures as well as in developing some novel applications in related fields.

Key Words—Heterostructure, Mesoporosity, Montmorillonite, Textural Evolution, Zerovalent Iron Nanoparticle.

INTRODUCTION

Heterostructures formed by nanoparticles embedded in porous hosts are of great interest for a variety of sorption-based applications of catalysis (Mitsudome *et al.*, 2007), decontamination (Yuan *et al.*, 2009), and gas purification (Lu *et al.*, 2009). Montmorillonite (Mt), as a naturally occurring micro- and mesoporous material, is an ideal host for synthesizing heterostructures in terms of its unique combination of cation exchange, intercalation, and swelling properties (Pinnavaia, 1983). In the dry state, a Mt system can be described by three structural units and by the arrangement of these units in space (Neaman *et al.*, 2003; Bergaya *et al.*, 2006). The first unit is the layer with thickness of ~1 nm and lateral extent of ~100–200 nm (Drummy *et al.*, 2005). The second unit is the particle arising from the short-range turbostratic stacking of layers along the *c* direction (Cadene *et al.*, 2005). The third unit is the aggregate consisting of a group of particles associated with each other by different modes (Benna *et al.*, 1999; Ramos-Tejada *et al.*, 2001). The arrangement of these units may provide Mt with interlayer, interparticle, and interaggregate pores of varied size and shape (Bergaya and Lagaly, 2006) and, thus, make Mt versatile at accommodating various nanoparticles.

Zerovalent iron (Fe^0) nanoparticles are of great physical and chemical importance and have attracted much attention in recent years for their magnetic (Grigorieva *et al.*, 2006) and catalytic (Yan *et al.*, 2008) properties, as well as their great potential in environmental remediation (Sarathy *et al.*, 2010). Nevertheless, these Fe nanoparticles are easy to agglomerate and to oxidize, which makes them difficult to prepare, study, and apply (Huber, 2005; Bomatí-Miguel *et al.*, 2006). Their oxidation can be conveniently minimized by coating them with native Fe-oxide shells. Their agglomeration can be largely inhibited by stabilizing them with various hosts, such as Mt. This porous clay mineral is, thus, expected to be suitable to stabilize Fe^0 nanoparticles and to enhance the performance of the materials obtained for pelletization,

* E-mail address of corresponding author:
yuanpeng@gig.ac.cn
DOI: 10.1346/CCMN.2011.0590506

storage, and transportation (Yuan *et al.*, 2009), as well as favoring the reuse and recycling of nanoparticles from reaction mixtures (Király *et al.*, 1996; Papp *et al.*, 2004). From this point of view, the Fe^0/Mt heterostructure is promising as an environment-friendly heterogeneous catalyst and as an effective adsorbent.

Textural characteristics are important in the practical applications of catalysts and adsorbents. The total surface area is crucial in determining the accessibility of reaction sites in catalysts and adsorbents. In catalysis and adsorption reactions, the pore architecture generally controls transport phenomena and governs selective properties. As a result, pore volume and pore-size distribution (PSD) are essential parameters in these reactions (Storck *et al.*, 1998). In this sense, elucidating the textural characteristics of Fe^0/Mt heterostructure, which controls its key properties when used in sorption-related fields, is of interest.

Conventionally, nitrogen physisorption is one of the best techniques to study the textural characteristics of solid materials (Sing *et al.*, 1985). This technique accurately determines the amount of nitrogen adsorbed on a solid material, and the isotherm obtained from adsorption measurements, combined with various computational models, can offer information on textural characteristics. Other techniques including ^{129}xenon-nuclear magnetic resonance (Tsiao *et al.*, 1998), transmission electron microscopy (TEM) (Groen *et al.*, 2003), atomic force microscopy (AFM) (Occelli *et al.*, 1994), X-ray diffraction (XRD) (He *et al.*, 2006), and small-angle neutron scattering (Pinnavaia *et al.*, 1984a) are also often used to complement the adsorption results and provide a more detailed picture of the porous and structural aspects of the materials under investigation.

The objectives of this study were to hybridize Fe^0 nanoparticles with the Mt host and to investigate the textural evolution of these heterostructures under different iron loadings. Fe^0/Mt heterostructures with different iron loadings were synthesized by impregnation of Mt by ferric ions followed by chemical reduction with sodium borohydride in solution. The nitrogen adsorption-desorption isotherms of samples were recorded and treated with different computational models to determine the textural characteristics. X-ray diffraction, microscopy, and elemental analyses were also carried out to complement the results obtained from the adsorption analyses.

MATERIALS AND METHODS

The starting Ca^{2+}-Mt was obtained from Inner Mongolia, China. The <2 μm fraction was collected by sedimentation. The cationic exchange capacity (CEC) was determined to be ~111 mmol/100 g according to the ammonium acetate saturation method (Mackenzie, 1951). Chemicals $FeCl_3 \cdot 6H_2O$ and $NaBH_4$ (Shanghai Jiachen Chemical Co., Ltd., China) were of analytical grade and used as received. Distilled water was used throughout this work.

Preparation of samples

Fe^0/Mt heterostructures were prepared by impregnation of Mt with Fe^{3+} solution followed by chemical reduction with $NaBH_4$ in solution. Typically, Ca^{2+}-Mt (2.0 g) was stirred in 100 mL of water for 24 h, and then $FeCl_3 \cdot 6H_2O$ was added to the aqueous clay dispersion with 1, 2, 4, and 6 times the CEC of Mt. The mixture was stirred for another 24 h and then 100 mL of freshly prepared $NaBH_4$ solution was added dropwise under stirring. The molar ratio of B to Fe was 4:1. After $NaBH_4$ was added, the solution turned black, indicating the reduction of ferric ions.

The pH of the Mt dispersion was measured before adding the $NaBH_4$ solution. All experiments were carried out at room temperature and no precautions were taken to eliminate oxygen from the reaction vessel. The dispersion was washed thoroughly by centrifugation/redispersion cycles in 50 vol.% aqueous ethanol solution then in anhydrous acetone, and vacuum dried at 60ºC for 24 h. The final product prepared at an Fe^{3+} amount equivalent to 1, 2, 4, or 6 times the CEC was labeled as MtFe^0-1, MtFe^0-2, MtFe^0-4, or MtFe^0-6, respectively. Reference samples of pure Fe^0 nanoparticles without clay and of Fe^{3+}-Mt without $NaBH_4$ reduction were prepared by the same procedure as for MtFe^0-6 and labeled as Fe^0 and as Fe^{3+}-Mt, respectively.

Characterization methods

Elemental analyses were performed on a Varian Vista-Pro inductively coupled plasma optical emission spectrometry (ICP-OES). The XRD patterns were recorded between 1.0 and 80º2θ at a continuous scanning speed of 4º2θ/min, using a Bruker D8 Advance diffractometer with CuKα radiation (λ = 0.154 nm) under target voltage 40 kV and current 30 mA.

Electron microscopic analyses were carried out using a combination of a 100 kV JEOL JEM-100CXII transmission electron microscope attached to an electron diffractometer, a 200 kV JEOL JEM-2100 high-resolution transmission electron microscope (HRTEM), and a 5 kV FEI-Sirion 200 field emission scanning electron microscope (FESEM) attached to an Oxford INCA energy dispersive X-ray spectrometer (EDX). The sample for TEM or HRTEM was prepared by sonication of the powders in ethanol. Then, a holey carbon-coated copper grid was dipped in the dispersion and allowed to air dry. The sample for FESEM was prepared by dispersing the powders in ethanol and then evaporating a drop of the dispersion on a copper conductive tape. No sputtering of the sample with gold was used in order to avoid possible confusion between the Fe and gold particles.

Textural analyses based on the nitrogen adsorption-desorption isotherms were conducted using a static volumetric Micromeritics ASAP 2020 system at 77 K.

Prior to measurement, samples were degassed at 333 K for 18 h under a residual pressure of $<10^{-3}$ Torr. The data points were collected in the relative pressure (p/p_0) range of 10^{-6}–0.99. To obtain an adequate characterization of the microporous region, sufficient data points at low pressures are necessary (Gil and Gandía, 2003). The Micromeritics ASAP 2020 built-in software was used for all computations based on isotherm data. The kinetic diameter of nitrogen was taken as 0.364 nm (Lin *et al.*, 2009).

RESULTS

Elemental analyses of samples

The elemental contents of Fe, Ca, Na, and Al were measured (Table 1). The method was not designed to measure structural Fe in Mt lattices, so it was excluded from the Fe contents. The Al contents were exclusively from the Mt lattices and no other Al was introduced to the samples. The Fe contents, determined by ICP-OES analyses, were approximately equal to the Fe loadings added initially (Table 1), reflecting the almost complete reduction of Fe^{3+} to Fe^0.

Zerovalent Fe nanoparticles/montmorillonite heterostructures

In comparison with the agglomerated pure Fe nanoparticles synthesized in the absence of Mt (Figure 1a), the hybridized Fe nanoparticles were well dispersed on the Mt surface (Figure 1b), taking $MtFe^0$-6 as a representative sample. The metallic nature of these hybridized Fe nanoparticles was revealed by the α-Fe (110) and (211) diffraction rings in the corresponding selected area electron diffraction (SAED) pattern (Figure 1c inset) and was also confirmed by the inner dark contrast of metallic Fe of these nanoparticles

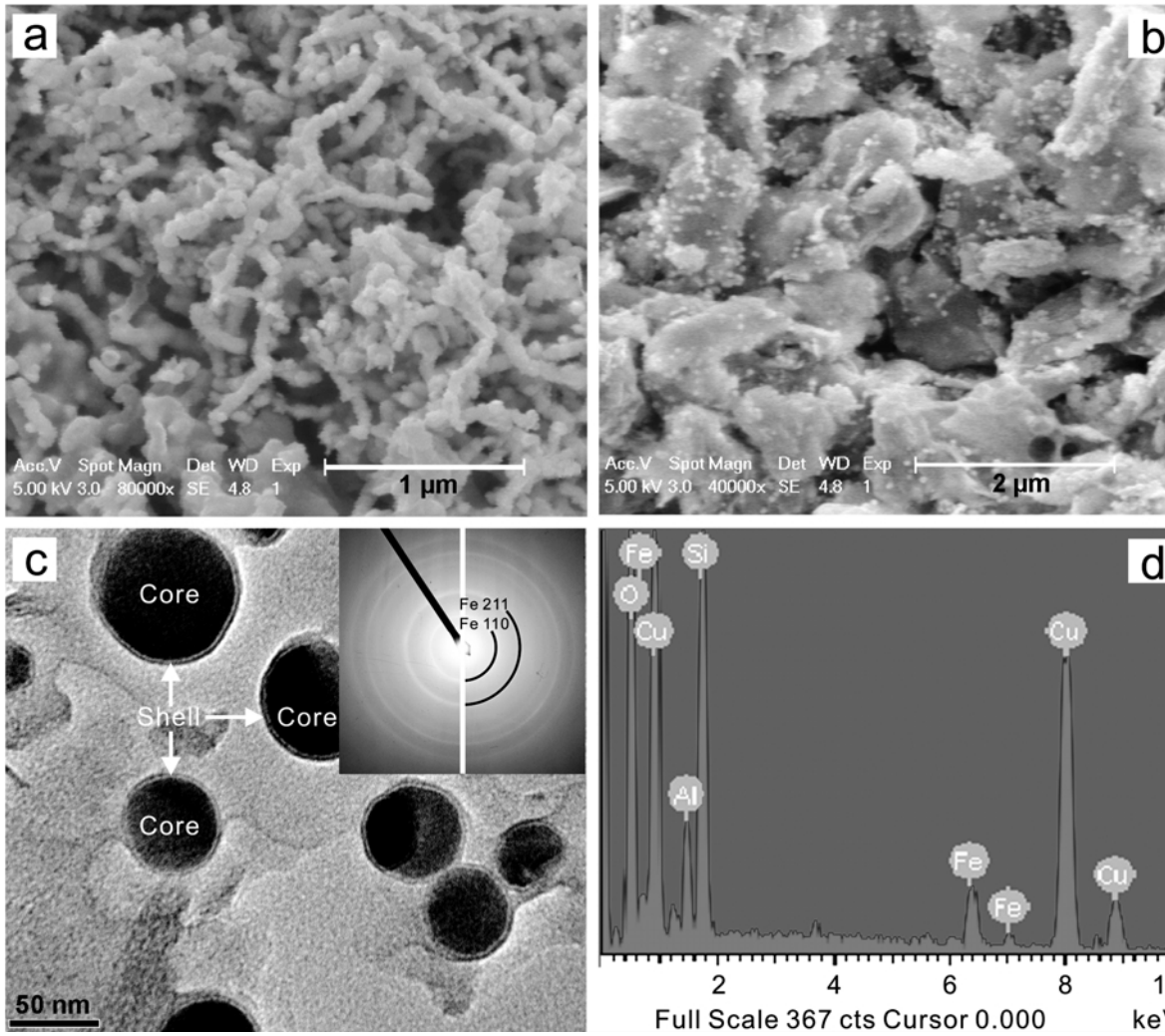

Figure 1. FESEM images of (a) Fe^0 nanoparticles and (b) $MtFe^0$-6. (c) High-magnification TEM image of $MtFe^0$-6 with the corresponding SAED pattern inset. (d) EDX spectrum of $MtFe^0$-6.

Table 1. Elemental contents (wt.%) of Ca^{2+}-Mt, Fe^{3+}-Mt, and $MtFe^0$-1−$MtFe^0$-6[a] and the medium pH values measured before adding the $NaBH_4$ solution.

Sample	Fe[b]	Ca	Na	Al	pH
Ca^{2+}-Mt	0	1.46	0.27	7.93	–
$MtFe^0$-1	2.23 (2.07)	1.41	0.81	7.80	2.51
$MtFe^0$-2	4.18 (4.14)	1.36	1.04	7.73	2.15
$MtFe^0$-4	8.07 (8.27)	1.26	1.02	7.30	1.96
$MtFe^0$-6	11.53 (12.41)	1.15	0.97	6.70	1.81
Fe^{3+}-Mt	6.04	<0.01	0.08	6.19	–

[a] Determined by ICP-OES analyses.
[b] The contribution of structural Fe of Mt lattices is excluded and the Fe loading added initially is indicated in parentheses.

(Figure 1c). The native Fe-oxide shells coating the Fe cores were clearly revealed by the outer bright contrast of these nanoparticles (Figure 1c). The corresponding Fe and O peaks in the EDX spectrum (Figure 1d) further confirmed the formation of the native Fe-oxide shells, where the Fe peaks were derived from both the α-Fe cores and the Fe-oxide shells, whereas the O peak was derived exclusively from the Fe-oxide shells. Interestingly, the Fe-oxide shells were almost invariably ~3 nm thick, independent of the particle size.

Furthermore, in the XRD patterns of Ca^{2+}-Mt and $MtFe^0$-1 to -6 (Figure 2) the reflections of $MtFe^0$-6 (as well as $MtFe^0$-1, -2, and -4) were similar to that of Ca^{2+}-Mt, not attributable to any Fe-related phases, indicating that the crystalline size of these Fe^0 nanoparticles was small and consequently did not show XRD lines. (In the present work, estimation of crystal size of Fe^0 nanoparticles was difficult, due to the absence of Fe-related XRD peaks.)

As a result, generalized to all the heterostructures, the hybridized Fe^0 nanoparticles composed of fine crystal grains were well dispersed on the Mt surface and were

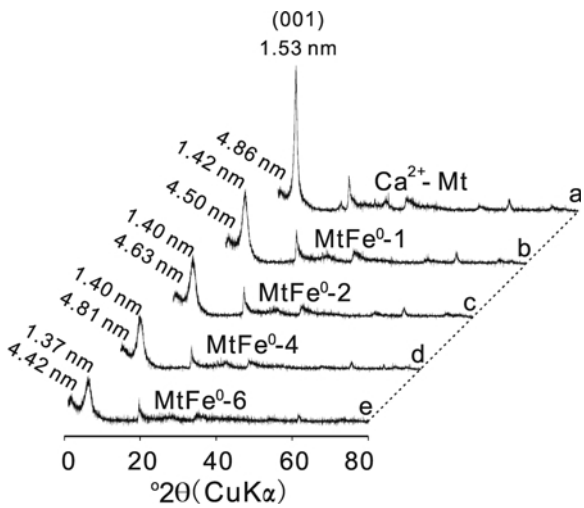

Figure 2. XRD patterns of (a) Ca^{2+}-Mt, (b) $MtFe^0$-1, (c) $MtFe^0$-2, (d) $MtFe^0$-4, and (e) $MtFe^0$-6.

resistant to oxidation under the protection of native Fe-oxide shells. Moreover, as revealed by the particle-size distributions obtained by analyzing at least 300 particles from the TEM images of each sample (the right panels of Figure 3a−d), the average size of these Fe^0 nanoparticles was affected by the Fe loadings. With increasing Fe loading, the average particle size increased statistically from 30 nm for $MtFe^0$-1 and 34 nm for $MtFe^0$-2 to 58 nm for $MtFe^0$-4 and 55 nm for $MtFe^0$-6.

Isotherms of samples

The N_2 adsorption-desorption isotherms (Figure 4) of Ca^{2+}-Mt and $MtFe^0$-1 to -6, as well as Fe^0 nanoparticles, revealed that the isotherm of Ca^{2+}-Mt was of type IV, with a characteristic hysteresis loop of type H3 in the IUPAC classification (Sing *et al.*, 1985), corresponding to capillary condensation taking place in slit-shaped mesopores. In addition, in the low p/p_0 region, the adsorption isotherm exhibited a distinct increase in the amount of nitrogen adsorbed, indicating the presence of micropores. The Ca^{2+}-Mt thus contained both micro- and mesopores. A forced closure occurred in the p/p_0 range of 0.47−0.50 along the desorption branch of the isotherm, which was attributed to the tensile strength effect often observed in smectite isotherms (Groen *et al.*, 2003; Auerbach *et al.*, 2004). The combined micro- and mesoporosity and the tensile strength effect were also observed for $MtFe^0$-1 to -6 because their isotherms were similar to those of Ca^{2+}-Mt. The adsorption-desorption isotherm of Fe^0 nanoparticles also revealed both micro- and mesopores, probably derived from the voids between the particles because Fe^0 nanoparticles themselves are non-porous.

Evolution of total surface area, total pore volume, and average pore diameter

The BET nitrogen adsorption method has been used widely to determine the total surface area (SA) of solid materials. For solid materials containing micropores, the three-parameter BET equation should be applied (Brunauer *et al.*, 1938, 1940; Gervasini, 1999). Thus, the adsorption data of Ca^{2+}-Mt and $MtFe^0$-1 to -6 were treated with the three-parameter BET equation in the p/p_0

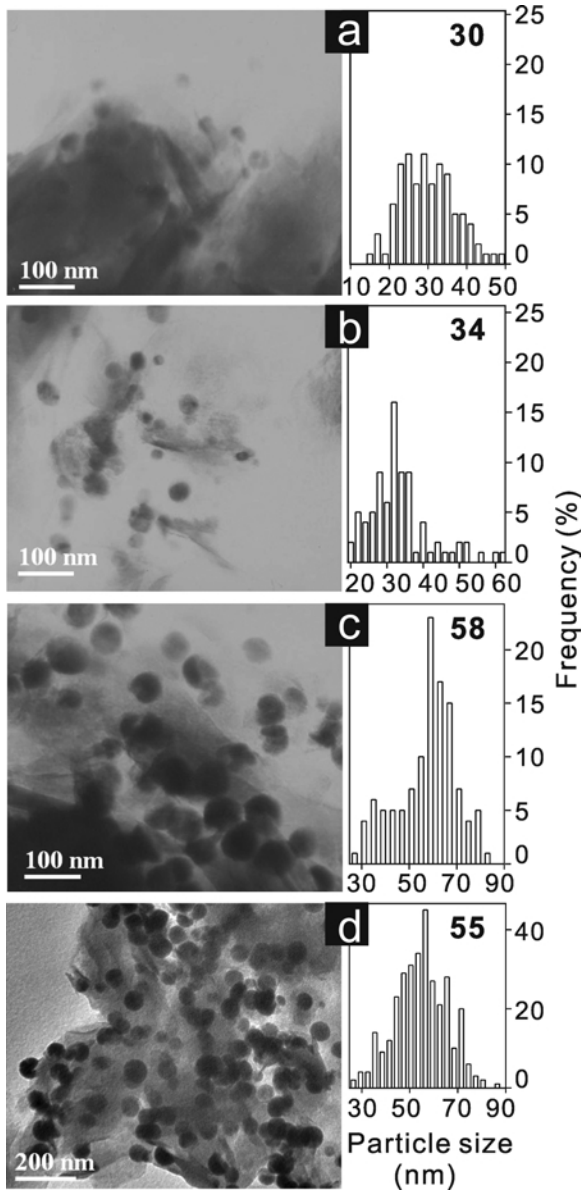

Figure 3. TEM images (left) and corresponding particle-size distributions (right panels) of (a) $MtFe^0$-1, (b) $MtFe^0$-2, (c) $MtFe^0$-4, and (d) $MtFe^0$-6. The inset numbers in the particle-size distributions are average particle sizes (nm) of Fe nanoparticles.

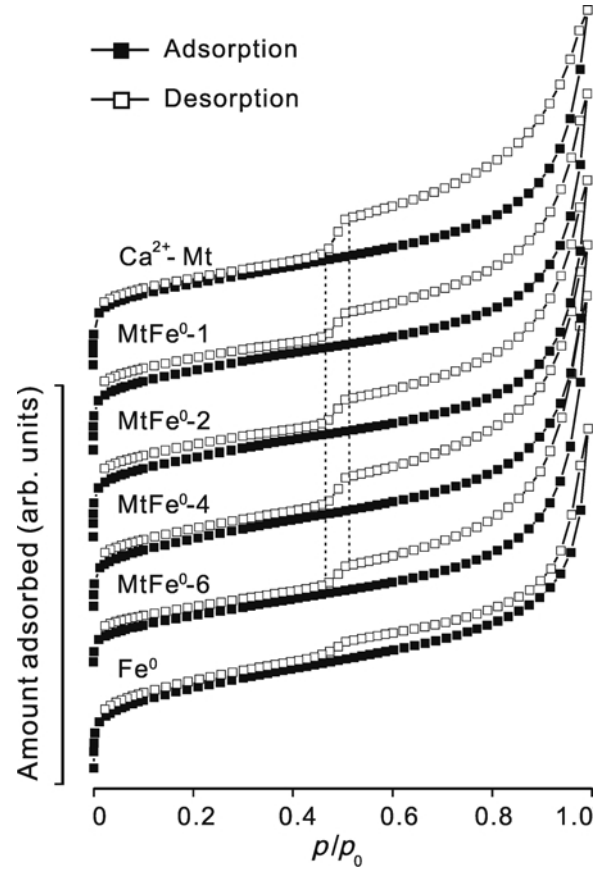

Figure 4. Nitrogen adsorption-desorption isotherms of Ca^{2+}-Mt, Fe^0 nanoparticles, and $MtFe^0$-1–$MtFe^0$-6 at 77 K.

range 0–0.4, in terms of SA, C_{BET} constant, and the maximum number of nitrogen layers adsorbed (n_{av}) (Table 2), using the Levenberg-Marquardt algorithm. This algorithm is iterative and has become a standard technique for nonlinear least-squares problems (Lourakis, 2005). For all the samples, the C_{BET} constants are positive and related exponentially to the heat of adsorption in the first adsorbed layer (Sing *et al.*, 1985) , indicating the validity of applying the three-parameter BET equation. The n_{av} values indicated that the microporous character was more pronounced for Ca^{2+}-Mt and $MtFe^0$-1 (n_{av} = 3.4 and 3.8, respectively) than for $MtFe^0$-2 and $MtFe^0$-4 (n_{av} = 5.8 and 5.1, respectively). $MtFe^0$-6 had the weakest microporous character with the n_{av} value as high as 17.5. The SA value of 78 m^2/g was obtained for Ca^{2+}-Mt, which is consistent with the literature values of Mt in a non-swelling state (Rutherford *et al.*, 1997; Séquaris *et al.*, 2002). For all heterostructures, the SA values were lower than that of Ca^{2+}-Mt and decreased as the Fe loadings increased.

The total pore volume (V_p) was assessed from the amount of nitrogen adsorbed at a relative pressure of 0.99. The average pore diameter (APD) was assessed by the classical Gurvitch rule, assuming cylindrical pore geometry (Gregg and Sing, 1982). Notably, in the calculation of the APD values, the corresponding SA values calculated by the three-parameter BET equation were involved. The total pore volumes for Ca^{2+}-Mt and $MtFe^0$-1 to -6 varied slightly at 0.121 ± 0.005 cm^3/g (Table 2), indicating that Fe loadings did not significantly affect the total pore volume. On the contrary, the Fe loadings clearly affected the APD. As the Fe loadings increased (from 0 CEC for Ca^{2+}-Mt to 6 CEC for $MtFe^0$-6), the APD increased almost linearly (Table 2).

Table 2. Textural properties derived from the nitrogen adsorption at 77 K of Ca^{2+}-Mt and $MtFe^0$-1−$MtFe^0$-6.

Sample	Surface area (m^2/g)	C_{BET}[a]	n_{av}[a]	V_p (total pore volume) (cm^3/g)	Average pore diameter (nm)	$S_{\mu DFT}$[b] (m^2/g)	S_{extDFT}[b] (m^2/g)	$V_{\mu pDFT}$[b] (cm^3/g)	V_{mpDFT}[b] (cm^3/g)	d_{PDFT}[b] (nm)
Ca^{2+}-Mt	78	2393	3.4	0.138	7.1	35	43	0.026	0.112	0.8;1.3
$MtFe^0$-1	68	3514	3.8	0.124	7.3	34	34	0.022	0.102	0.8;1.1;1.3
$MtFe^0$-2	56	1699	5.8	0.126	8.5	23	33	0.019	0.107	1.0;1.3
$MtFe^0$-4	48	1555	5.1	0.115	9.5	19	29	0.015	0.100	1.1;1.3
$MtFe^0$-6	41	643	17.5	0.120	11.6	17	24	0.013	0.107	1.1;1.3

[a] C_{BET} constant and maximum number of nitrogen layers adsorbed (n_{av}), evaluated from the three-parameter BET equation. [b] Micropore surface area ($S_{\mu DFT}$), external surface area (S_{extDFT}), micropore volume ($V_{\mu pDFT}$), mesopore volume (V_{mpDFT}), and maxima of micropore-size distribution (d_{PDFT}) evaluated using the DFT method.

Evolution of microporosity

The density functional theory (DFT) method, as a result of the development of statistical mechanics, is sophisticated and effective for determining the microporous character of materials (Quirke and Tennison, 1996; Zeng *et al.*, 2009; Johnson *et al.*, 1997). The microporosities of Ca^{2+}-Mt and $MtFe^0$-1 to -6 were assessed by the DFT method in which the p/p_0 range was limited at 0−0.05 corresponding to pore diameters of <2 nm and the pore geometry was set as a slit. The DFT fittings to the experimental adsorption data (Figure 5) were good over the selected, as well as the whole, p/p_0 range for all the samples, which guaranteed the reliability of the assessment. The micropore surface area ($S_{\mu DFT}$) as well as the micropore volume ($V_{\mu pDFT}$) obtained by the DFT method decreased gradually from Ca^{2+}-Mt to $MtFe^0$-6 as the Fe loadings increased (Table 2).

A further detailed description of the microporous character can be realized by studying the micropore-size distribution of different samples (Figure 6) according to the DFT method. Considering that the presence of mesopores in combined micro- and mesoporous materials tends to introduce into the micropore-size distributions artificial peaks which are typically broad and diffuse (Groen *et al.*, 2003), only the sharp and symmetrical peaks were believed to reflect the exact porous properties for Ca^{2+}-Mt and $MtFe^0$-1 to -6 located below 1.4 nm and for Fe^0 nanoparticles located below 1.0 nm. The maxima of the micropore-size distributions (d_{PDFT}) for Ca^{2+}-Mt and $MtFe^0$-1 to -6 (Table 2) revealed that the starting Ca^{2+}-Mt with no Fe loading yielded a bimodal pore-size distribution with maxima at 0.8 and 1.3 nm (Figure 6a). After being loaded with Fe amounts equivalent to 1 CEC, an additional maximum at 1.1 nm was observed for MFe^0-1, and the maxima at 0.8 and 1.3 nm remained. Compared with Ca^{2+}-Mt, the 0.8 nm micropore volume increased whereas the 1.3 nm micropore volume decreased (Figure 6a,b). With further increases in Fe loadings, the maximum at 0.8 nm disappeared for $MtFe^0$-2, -4, and -6, the maximum at 1.1 nm shifted to 1.0 nm for $MtFe^0$-2 and remained for $MtFe^0$-4 and -6, and the maximum at 1.3 nm remained for $MtFe^0$-2, -4, and -6; the 1.1 and 1.3 nm micropore volumes decreased from $MtFe^0$-1 to -6 (Figures 6b−e), respectively. As for Fe^0 nanoparticles, one maximum at 0.9 nm was recognized (Figure 6f).

Evolution of mesoporosity

The DFT method can be applied to pores ranging from micro- to meso-sizes (Elsayed *et al.*, 2007). The mesoporosities of Ca^{2+}-Mt and $MtFe^0$-1 to -6 were

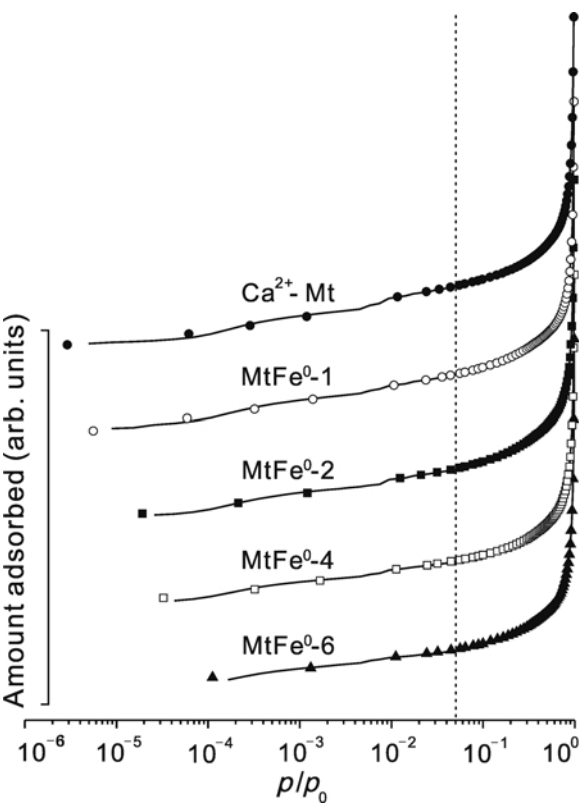

Figure 5. DFT fits (solid lines) to experimental adsorption data (dots) of Ca^{2+}-Mt and $MtFe^0$-1−$MtFe^0$-6.

assessed by the DFT method, in the same way as for the microporosities, except that the p/p_0 range was extended to the mesoporous region. The reliability of experimental results for all samples was considered to be good, as shown by the fitting to isotherm models (Figure 5). Also, the experimental results were calculated using the adsorption branches, to avoid the influence of tensile strength effect (Groen *et al.*, 2003). The mesopore volume (V_{mpDFT}), obtained by subtracting the micropore volume ($V_{\mu pDFT}$) from the total pore volume (V_p), was insensitive to the Fe loadings (Table 2); but the external surface area (S_{extDFT}), obtained by subtracting the micropore surface area ($S_{\mu DFT}$) from the total surface area (*SA*), decreased from Ca^{2+}-Mt to $MtFe^0$-6. The DFT-derived mesopore-size distributions of Ca^{2+}-Mt (Figure 7) to some extent exhibited a random character, in which pores of different sizes coexisted (Figure 7a). Compared with the pore-size distribution of the unloaded Ca^{2+}-Mt, the mesoporous region was unaffected by the Fe loadings for $MtFe^0$-1 to -6 (Figures 7b–e). The pure Fe reference also exhibited a broad distribution with pores of different sizes (Figure 7f).

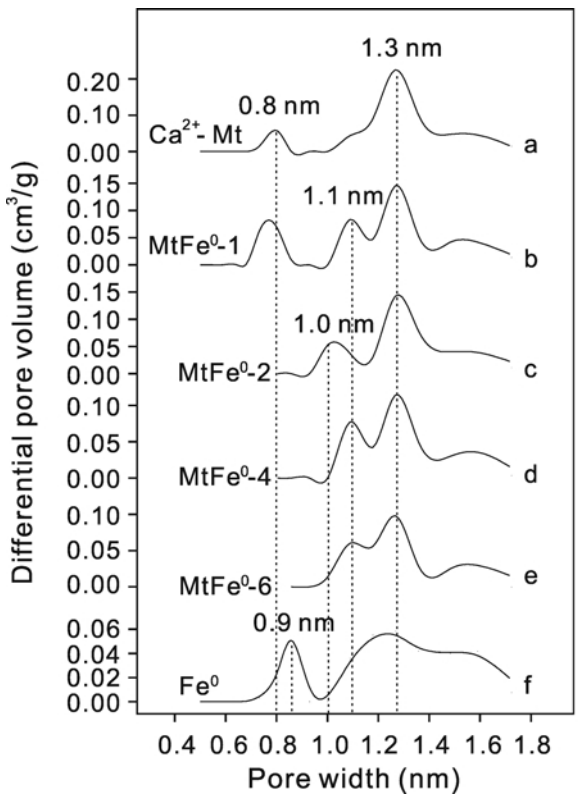

Figure 6. DFT micropore-size distributions of (a) Ca^{2+}-Mt, (b) $MtFe^0$-1, (c) $MtFe^0$-2, (d) $MtFe^0$-4, (e) $MtFe^0$-6, and (f) Fe^0 nanoparticles.

DISCUSSION

As the Fe loadings increased for all the heterostructures, the Fe^0 nanoparticles exhibited an improved dispersivity (the left panels of Figure 3a–d) which would be attributed to the dispersing action of the Mt particles. The clay mineral favored and controlled the heterogeneous nucleation of Fe clusters, preventing their mutual contact. Increasing Fe loadings is expected to make the dispersing action of fixed amounts of Mt less effective and, consequently, to promote the formation of large particles.

Hybridized Fe nanoparticles were, moreover, highly resistant to oxidation due to protection afforded by native Fe-oxide shells which had an almost invariable thickness of ~3 nm regardless of the Fe particle size. This constant thickness may be explained by the Caberra-Mott theory (Fung *et al.*, 2000; Wang *et al.*, 2005). According to this theory, upon the initial attachment of oxygen to the surface of Fe and the formation of a thin oxide layer, the electron tunnels through the thin oxide layer and ionizes the oxygen, leading to an electrical field between the Fe and the surface of the oxide layer. The electrical field then drives the outward diffusion of the ionized Fe. At room temperature, ~0.2 fs are needed to form an initial 1 nm thick oxide layer on a freshly exposed Fe surface, 40 s for 2 nm, 40 weeks for 3 nm, and 600 y for 4 nm (Fung *et al.*, 2000; Wang *et al.*, 2005). Considering that the Fe nanoparticles in the present study were formed at room temperature and the period of time from formation to microscopic imaging was <40 weeks, the Fe-oxide shells should have been <~3 nm thick

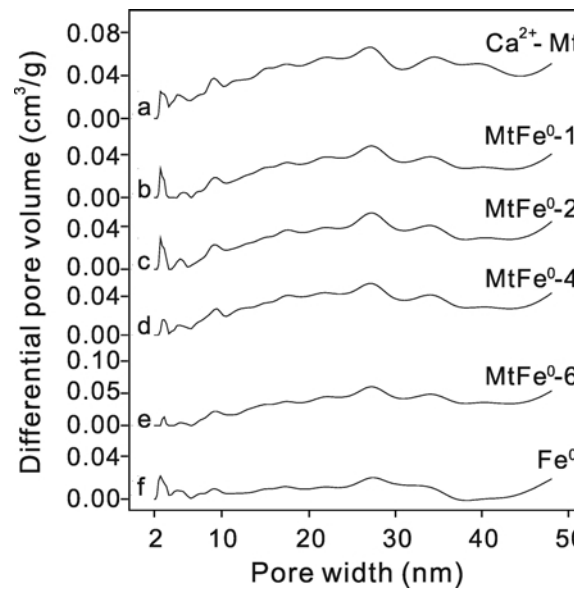

Figure 7. DFT mesopore-size distributions of (a) Ca^{2+}-Mt, (b) $MtFe^0$-1, (c) $MtFe^0$-2, (d) $MtFe^0$-4, (e) $MtFe^0$-6, and (f) Fe^0 nanoparticles.

Ca^{2+}-Mt exhibited an intense (001) reflection at ~5.8º2θ (Figure 2a). After loading with Fe, the (001) reflection was also observed for $MtFe^0$-1 to -6 (Figure 2b−e), indicating that the lamellar structure of Mt was retained. Nevertheless, compared with Ca^{2+}-Mt, the d_{001} basal spacings of $MtFe^0$-1 to -6 decreased from 1.53 to 1.37 nm (Figure 2a−e), revealing some changes in the interlayer space of Mt. Also, the intensity of the (001) reflection decreased from Ca^{2+}-Mt to $MtFe^0$-6 with increasing Fe loadings (Figure 2a−e), indicating some disturbances of the lamellar structure. These disturbances may have been caused by intercalation of fine clusters into the interlayer space of Mt, as reported by Mastalir *et al*. (2002) and Papp *et al*. (2004), and by structural destruction of Mt layers as reported by Shinoda *et al*. (1995) and Temuujin *et al*. (2004). Slight structural destruction of Mt layers was confirmed by the decreased Al contents from Ca^{2+}-Mt to $MtFe^0$-6 (Table 1), which was probably the result of Al(III) release from Mt lattices under acid attack. The protons were derived from the hydrolysis of Fe^{3+} before sodium borohydride reduction, which decreased the pH with increasing Fe loading (Table 1).

The absence of intercalation of fine clusters in the interlayer space of Mt was confirmed by tracking the element contents of samples at different synthesis stages. This tracking method can be illustrated using, as an example, $MtFe^0$-6 formed from Ca^{2+}-Mt (Figure 8). The Ca^{2+} content of Ca^{2+}-Mt was much greater than the Na^+ content (Table 1), thus Ca^{2+} initially dominated the interlamellar exchange sites. Fe^{3+}-Mt was then formed by almost complete ion exchange with Fe^{3+}, causing interlamellar Ca^{2+} and Na^+ to become almost negligible (Table 1). Subsequent chemical reduction converted the Fe^{3+}-Mt to $MtFe^0$-6, in which the Fe content increased further and the sum of Ca^{2+} and Na^+ contents became greater than in the starting Ca^{2+}-Mt, although the relative amounts of Ca^{2+} *vs.* Na^+ decreased (Table 1) due to the addition of the reducing agent (sodium borohydride). This regeneration process was proposed by Zhang and Manthiram (1996). The greater amount of interlamellar Na^+ could account for the smaller d_{001} spacing observed in $MtFe^0$-6 than in Ca^{2+}-Mt. The regeneration of interlayer Ca^{2+} and Na^+ ions was at the expense of expelling Fe^{3+} from the interlayer space. These expelled Fe^{3+} ions were then reduced to Fe^0 outside the interlayer space of Mt, leading to a greater Fe content in $MtFe^0$-6 than in Fe^{3+}-Mt revealing clearly the exclusion of Fe^0 intercalation. Further evidence of the lack of Fe^0 intercalation was the relative similarity of the d_{001} spacings among samples $MtFe^0$-1 to -6 (Figure 2b−e).

In these Fe^0/Mt heterostructures, metallic Fe was not intercalated into the interlayer space of Mt but was located mainly on the external surface of the Mt. This was visualized by electron microscopic imaging (Figure 1b,c and the left panels of Figure 3a−d). Also, in the TEM images of $MtFe^0$-1 to -6 the random arrangement of Mt and Fe nanoparticles is shown (the left panels of Figure 3a−d), which may correspond to the partially disordered structure of Mt as revealed by the XRD analyses. This partially disordered structure of Mt could be described as a 'card-house' caused by edge-to-face and/or edge-to-edge associations of clay particles (Benna *et al.*, 1999). The 'card-house' structure was previously reported for Al-pillared interlayered clay by Pinnavaia *et al.* (1984b) and characterized by a broad PSD and an absent or broadened (001) XRD reflection (Occelli *et al.*, 1987). Recently, a broad XRD peak at a very low 2θ angle has also been cited as evidence for the 'card-house' arrangement in mesoporous structures (Clinard *et al.*, 2003; Bergaya *et al.*, 2005; Yuan *et al.*, 2006a, 2006b). Therefore, the broad mesopore-size distributions (Figure 7b−e) and the broad XRD peaks with d spacings >4.4 nm at ~1.8º2θ for $MtFe^0$-1 to -6 (Figure 2b−e) further confirmed the formation of the 'card-house' structure. In this case, the external surfaces define the interparticle pores (He *et al.*, 2006). Consequently, for all the heterostructures studied, the Fe^0 nanoparticles could be considered to occupy the interparticle pores of Mt equally, as visualized by the FESEM imaging of $MtFe^0$-6, for example (Figure 1b), and by schematic representation (Figure 9).

Taking into account the discussion above, the influence of Fe loadings on the textural characteristics of Fe^0/Mt heterostructures may be attributed to the number and size of the Fe^0 nanoparticles as well as to their dispersion in the 'card-house' structure of Mt. In the starting Ca^{2+}-Mt without Fe loading, the 'card-house' structure also formed, as revealed by the broad mesopore-size distribution (Figure 7a) and by the broad

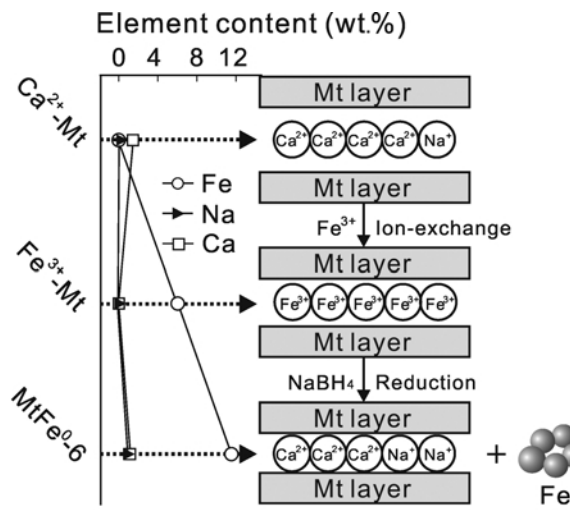

Figure 8. Schematic illustration tracing the element contents from Ca^{2+}-Mt to Fe^{3+}-Mt−$MtFe^0$-6. After impregnation, ferric ions were dominant as interlamellar cations of Mt. During the subsequent reduction process, Ca and Na ions regenerated in the interlayer space of Mt, with ferric ions being expelled and finally reduced to Fe^0 outside the interlayer space of Mt.

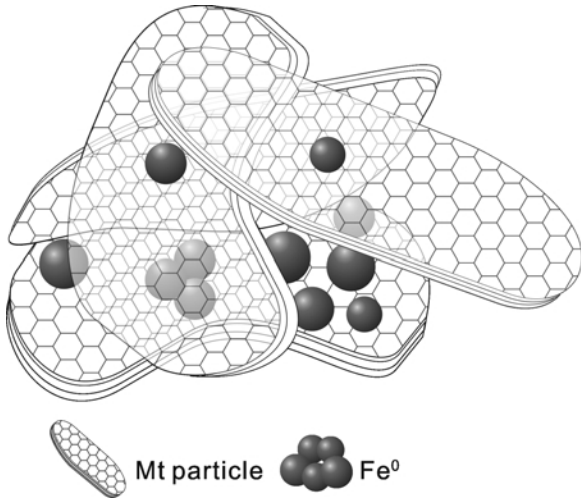

Figure 9. Schematic representation of the Fe^0/Mt heterostructure with Fe^0 nanoparticles filling the micro- and mesopores derived from the interparticle space of the 'card-house' structure of Mt.

XRD peak with *d* spacing of 4.9 nm (Figure 2a). After loading with Fe, the interparticle pores of the 'card-house' Mt structure were occupied by Fe^0 particles the number and size of which grew progressively from $MtFe^0$-1 to -6 (Table 1). Presumably, larger and more numerous Fe^0 nanoparticles would be expected to occupy a larger space and prop the clay particles further apart. As a result, with increased Fe loadings, the interparticle pores should tend to increase with increased APD values from Ca^{2+}-Mt to $MtFe^0$-6. In reality, however, a greater APD did increase the total pore volume but it varied only slightly among samples Ca^{2+}-Mt and $MtFe^0$-1 to -6, which is consistent with the formation of Fe^0 nanoparticles outside the Mt interlayers. The micropore volumes of Ca^{2+}-Mt and $MtFe^0$-1 to -6 were much smaller than the total pore volumes (Table 2). Thus, with the almost unchanged total pore volumes, the fluctuation of the micropore volumes affected slightly the mesopore volumes calculated by subtracting the micropore volumes from the total pore volumes, which rendered the mesopore volumes almost unchanged (Table 2). Moreover, as the Fe loadings increased, the Fe^0 nanoparticles in the interparticle pores of Mt tended to become larger and more numerous, which would make the pores less accessible by N_2 molecules. As a result, the number of the adsorption sites accessible by N_2 tended to decrease and the calculated total, micropore, and external surface areas decreased (Table 2)

The microporosities of Ca^{2+}-Mt and $MtFe^0$-1 to -6 were sensitive to the Fe loadings, which changed micropore-size distributions (Figure 6) and decreased micropore volumes from Ca^{2+}-Mt to $MtFe^0$-6 (Table 2). This could be attributed to the micropore filling by Fe^0 nanoparticles. Notably, in the PSD curves of $MtFe^0$-1 to -6 (Figure 6b–e) the peak at 0.9 nm assigned to the agglomeration of Fe^0 nanoparticles (Figure 6f) diminished, reflecting the almost complete loss of interparticle pores of Fe^0 nanoparticles and offering further evidence to confirm the improved dispersal of these hybridized Fe^0 nanoparticles. Because the interparticle pores of Fe^0 nanoparticles were almost completely lost, the source of microporosity in these heterostructures may have been derived from either the space between Mt particles or from the interlayer space between Mt layers. By subtracting the thickness of the Mt layer of ~1 nm from the corresponding d_{001} spacings (as indicated in Figure 2a–e), the interlayer heights of 0.53, 0.42, 0.40, 0.40, and 0.37 nm were calculated for Ca^{2+}-Mt and $MtFe^0$-1 to -6, respectively. These heights were larger than the kinetic diameter of nitrogen of 0.364 nm, which made possible the accessibility of the interlayer space to nitrogen. Based on this possibility, the micropores derived from the interlayer space should be insensitive to Fe loading because the interlayer space was free from the intercalation of Fe^0 nanoparticles. The observed microporosities were, however, sensitive to Fe loading, which leads to the deduction that the interlayer space is excluded as the source of microporosity. The inaccessibility of the interlayer space to nitrogen may be caused by the collapse of Mt layers during the vacuum degassing treatment. Thus, the micropores of these heterostructures were derived from the interparticle space of Mt and may be related to the staggering of particle edges and the overlap of particle regions, as proposed by Rutherford *et al.* (1997). When Mt was loaded with Fe at 1 CEC, a limited number of Fe^0 nanoparticles formed. A larger number of Fe^0 nanoparticles was expected to fill the larger micropores of Ca^{2+}-Mt centered at 1.3 nm (Figure 6a) whereas a smaller number of these Fe^0 nanoparticles was expected to fill the smaller micropores of Ca^{2+}-Mt centered at 0.8 nm (Figure 6a). Larger numbers of Fe^0 nanoparticles resulted in the partition of the initial micropores present at 1.3 nm in Ca^{2+}-Mt into two micropores centered at 1.1 and 1.3 nm, respectively, in $MtFe^0$-1 (Figure 6b). Due to being filled by Fe^0 nanoparticles, the 1.3 nm micropore volume decreased in comparison with Ca^{2+}-Mt. A smaller number of Fe^0 nanoparticles partitioned the 0.8 nm micropores into smaller sizes with increased micropore numbers. As the Fe loadings increased further, the size and number of Fe^0 nanoparticles increased. Consequently, the 0.8 nm micropores disappeared for $MtFe^0$-2, -4, and -6 (Figure 6c–e) due to the blocking by sufficient Fe^0 nanoparticles and the 1.1 and 1.3 nm micropores remained but with decreased differential pore volumes due to the filling by increased Fe^0 nanoparticles from $MtFe^0$-2 to $MtFe^0$-6 (Figure 6c–e).

In addition, the mesoporous to microporous volume ratios can be used as practical parameters to follow the evolution of pore structures as proposed by Gervasini (1999). The ratios of 4.31, 4.64, 5.63, 6.67, and 8.23

were obtained for Ca^{2+}-Mt, $MtFe^0$-1 to -6, respectively. The increased ratios indicated that the mesoporous character was enhanced as the Fe loadings increased, which was consistent with the weakened microporous character from Ca^{2+}-Mt to $MtFe^0$-6 as revealed by the n_{av} values discussed above.

CONCLUSIONS

Fe^0/Mt heterostructures with various Fe loadings were synthesized in aqueous solution. The hybridized Fe^0 nanoparticles were resistant to oxidation with an Fe-Fe oxide core-shell structure and were well dispersed and size-adjustable due to the dispersing action of Mt. Iron loading led to a 'card-house' Mt structure.

Under different Fe loadings, the textural evolution of the heterostructures formed was caused by the filling of the Mt 'card-house' structure by Fe^0 nanoparticles. Increasing the Fe loadings led to: (1) decreases in the total, micropore, and external surface areas, and also in the micropore volume; and (2) an increase in the average pore diameter. Nevertheless, the total pore and mesopore volumes remained almost unchanged.

In addition, as the Fe loadings increased, the mesoporous character of these heterostructures tended to be enhanced. Consequently, the Fe^0 nanoparticles became easily accessible allowing these nanosized heterostructures to be potentially useful in the fields of adsorption, heterogeneous catalysis, and environmental remediation.

ACKNOWLEDGMENTS

This work was funded by National Natural Science Foundation of China (Grant No. 40672036), Natural Science Foundation of Inner Mongolia (Grant No. 2010BS0606), and the Key Project of Chinese Ministry of Education (Grant No. 211028). The present study was a contribution (No. IS1295) from GIGCAS. The authors thank Prof. Aihua Yuan and Dr Dongxiao Wu for their help with TEM measurements.

REFERENCES

Auerbach, S.M., Carrado, K.A., and Dutta, P.K. (2004) *Handbook of Layered Materials*. Marcel Dekker, New York.

Benna, M., Kbir-Ariguib, N., Magnin, A., and Bergaya, F. (1999) Effect of pH on rheological properties of purified sodium bentonite suspensions. *Journal of Colloid and Interface Science*, **218**, 442−455.

Bergaya, F. and Lagaly, G. (2006) General Introduction: Clays, Clay Minerals, and Clay Science. Pp. 1−18 in: *Handbook of Clay Science* (F. Bergaya, B.K.G. Theng, and G. Lagaly, editors). Developments in Clay Science, **1**, Elsevier, Amsterdam.

Bergaya, F., Mandalia, T., and Amigouët, P. (2005) A brief survey on CLAYPEN and nanocomposites based on unmodified PE and organo-pillared clays. *Colloid & Polymer Science*, **283**, 773−782.

Bergaya, F., Theng, B.K.G., and Lagaly, G. (2006) *Handbook of Clay Science.* Developments in Clay Science, **1**. Elsevier, Amsterdam.

Bomatí-Miguel, O., Tartaj, P., Morales, M.P., Bonville, P., Golla-Schindler, U., Zhao, X.Q., and Veintemillas-Verdaguer, S. (2006) Core-shell iron-iron oxide nanoparticles synthesized by laser-induced pyrolysis. *Small*, **2**, 1476−1483.

Brunauer, S., Emmett, P.H., and Teller, E. (1938) Adsorption of gases in multimolecular layers. *Journal of the American Chemical Society*, **60**, 309−319.

Brunauer, S., Deming, L.S., Deming, W.E., and Teller, E. (1940) On a theory of the van der Waals adsorption of gases. *Journal of the American Chemical Society*, **62**, 1723−1732.

Cadene, A., Durand-Vidal, S., Turq, P., and Brendle, J. (2005) Study of individual Na-montmorillonite particles size, morphology, and apparent charge. *Journal of Colloid and Interface Science*, **285**, 719−730.

Clinard, C., Mandalia, T., Tchoubar, D., and Bergaya, F. (2003) HRTEM image filtration: nanostructural analysis of a pillared clay. *Clays and Clay Minerals*, **51**, 421−429.

Drummy, L.F., Koerner, H., Farmer, K., Tan, A., Farmer, B.L., and Vaia, R.A. (2005) High-resolution electron microscopy of montmorillonite and montmorillonite/epoxy nanocomposites. *Journal of Physical Chemistry B*, **109**, 17868−17878.

Elsayed, M.A., Hall, P.J., and Heslop, M.J. (2007) Preparation and structure characterization of carbons prepared from resorcinol-formaldehyde resin by CO_2 activation. *Adsorption*, **13**, 299−306.

Fung, K.K., Qin, B.X., and Zhang, X.X. (2000) Passivation of α-Fe nanoparticle by epitaxial γ-Fe_2O_3 shell. *Materials Science and Engineering A*, **286**, 135−138.

Gervasini, A. (1999) Characterization of the textural properties of metal loaded ZSM-5 zeolites. *Applied Catalysis A: General*, **180**, 71−82.

Gil, A. and Gandía, L.M. (2003) Microstructure and quantitative estimation of the micropore-size distribution of an alumina-pillared clay from nitrogen adsorption at 77 K and carbon dioxide adsorption at 273 K. *Chemical Engineering Science*, **58**, 3059−3075.

Gregg, S.J. and Sing, K.S.W. (1982) *Adsorption, Surface Area and Porosity*. Academic Press, London.

Grigorieva, N.A., Grigoriev, S.V., Eckerlebe, H., Eliseev, A.A., Napolskii, K.S., Lukashin, A.V., and Tretyakov, Yu.D. (2006) Magnetic properties of iron nanoparticles in mesoporous silica matrix. *Journal of Magnetism and Magnetic Materials*, **300**, e342−e345.

Groen, J.C., Peffer, L.A.A., and Pérez-Ramírez, J. (2003) Pore size determination in modified micro- and mesoporous materials. Pitfalls and limitations in gas adsorption data analysis. *Microporous and Mesoporous Materials*, **60**, 1−17.

He, H., Zhou, Q., Martens, W.N., Kloprogge, T.J., Yuan, P., Xi, Y., Zhu, J., and Frost, R.L. (2006) Microstructure of $HDTMA^+$-modified montmorillonite and its influence on sorption characteristics. *Clays and Clay Minerals*, **54**, 689−696.

Huber, D.L. (2005) Synthesis, properties, and applications of iron nanoparticles. *Small*, **1**, 482−501.

Johnson, S.A., Brigham, E.S., Ollivier, P.J., and Mallouk, T.E. (1997) Effect of micropore topology on the structure and properties of zeolite polymer replicas. *Chemistry of Materials*, **9**, 2448−2458.

Király, Z., Dékány, I., Mastalir, Á., and Bartók, M. (1996) In situ generation of palladium nanoparticles in smectite clays. *Journal of Catalysis*, **161**, 401−408.

Lin, C.C.H., Sawada, J.A., Wu, L., Haastrup, T., and Kuznicki, S.M. (2009) Anion-controlled pore size of titanium silicate molecular sieves. *Journal of the American Chemical Society*, **131**, 609−614.

Lourakis, M.I.A. (2005) A brief description of the Levenberg-Marquardt algorithm implemented by levmar. Institute of Computer Science Foundation for Research and Technology, Greece, http://www.ics.forth.gr/~lourakis/levmar/levmar.pdf

Lu, C.Y., Wei, M.C., Chang, S.H., and Wey, M.Y. (2009) Study of the activity and backscattered electron image of Pt/CNTs prepapared by the polyol process for flue gas purification. *Applied Catalysis A: General*, **354**, 57–62.

Mackenzie, R.C.A. (1951) Micromethod for determination of CEC of clay. *Journal of Colloid Science*, **6**, 219–222.

Mastalir, Á., Szöllösi, Gy., Király, Z., and Rázga, Zs. (2002) Preparation and characterization of platinum nanoparticles immobilized in dihydrocinchonidine-modified montmorillonite and hectorite. *Applied Clay Science*, **22**, 9–16.

Mitsudome, T., Nose, K., Mori, K., Mizugaki, T., Ebitani, K., Jitsukawa, K., and Kaneda, K. (2007) Montmorillonite-entrapped sub-nanoordered Pd clusters as a heterogeneous catalyst for allylic substitution reactions. *Angewandte Chemie International Edition*, **46**, 3288–3290.

Neaman, A., Guillaume, D., Pelletier, M., and Villiéras, F. (2003) The evolution of textural properties of Na/Ca-bentonite following hydrothermal treatment at 80 and 300ºC in the presence of Fe and/or Fe oxides. *Clay Minerals*, **38**, 213–223.

Occelli, M.L., Landau, S.D., and Pinnavaia, T.J. (1987) Physicochemical properties of a delaminated clay cracking catalyst. *Journal of Catalysis*, **104**, 331–338.

Occelli, M.L., Gould, S.A.C., and Drake, B. (1994) Atomic scale imaging of pillared rectorite catalysts with the atomic force microscope. *Microporous Materials*, **2**, 205–215.

Papp, S., Szél, J., Oszkó, A., and Dékány, I. (2004) Synthesis of polymer-stabilized nanosized rhodium particles in the interlayer space of layered silicates. *Chemistry of Materials*, **16**, 1674–1685.

Pinnavaia, T.J. (1983) Intercalated clay catalysts. *Science*, **220**, 365–371.

Pinnavaia, T.J., Rainey, V., Tzou, M.S., and White, J.W. (1984a) Characterisation of pillared clays by neutron scattering. *Journal of Molecular Catalysis*, **27**, 213–224.

Pinnavaia, T.J., Tzou, M.S., Landau, S.D., and Raythatha, R.H. (1984b) On the pillaring and delamination of smectite clay catalysts by polyoxo cations of aluminum. *Journal of Molecular Catalysis*, **27**, 195–212.

Quirke, N. and Tennison, S.R.R. (1996) The interpretation of pore size distributions of microporous carbons. *Carbon*, **34**, 1281–1286.

Ramos-Tejada, M.M., Arroyo, F.J., Perea, R., and Durán, D.G. (2001) Scaling behavior of the rheological properties of montmorillonite suspensions: correlation between interparticle interaction and degree of flocculation. *Journal of Colloid and Interface Science*, **235**, 251–259.

Rutherford, D.W., Chiou, C.T., and Eberl, D.D. (1997) Effects of exchanged cation on the microporosity of montmorillonite. *Clays and Clay Minerals*, **45**, 534–543.

Sarathy, V., Salter, A.J., Nurmi, J.T., Johnson, G.O., Johnson, R.L., and Tratnyek, P.G. (2010) Degradation of 1,2,3-trichloropropane (TCP): hydrolysis, elimination, and reduction by iron and zinc. *Environmental Science & Technology*, **44**, 787–793.

Séquaris, J.M., Camara Decimavilla, S., and Corrales Ortega, J.A. (2002) Polyvinylpyrrolidone adsorption and structural studies on homoionic Li-, Na-, K-, and Cs-montmorillonite colloidal suspensions. *Journal of Colloid and Interface Science*, **252**, 93–101.

Shinoda, T., Onaka, M., and Izumi, Y. (1995) Proposed models of mesopore structures in sulfuric acid-treated montmorillonites and K10. *Chemistry Letters*, **24**, 495–496.

Sing, K.S.W., Everett, D.H., Haul, R.A.W., Moscou, L., Pierotti, R.A., Rouquerol, J., and Siemieniewska, T. (1985) Reporting physisorption data for gas/solid systems with special reference to the determination of surface area and porosity. *Pure and Applied Chemistry*, **57**, 603–619.

Storck, S., Bretinger, H., and Maier, W.F. (1998) Characterization of micro- and mesoporous solids by physisorption methods and pore-size analysis. *Applied Catalysis A: General*, **174**, 137–146.

Temuujin, J., Jadambaa, Ts., Burmaa, G., Erdenechimeg, Sh., Amarsanaa, J., and MacKenzie, K.J.D. (2004) Characterisation of acid activated montmorillonite clay from Tuulant (Mongolia). *Ceramics International*, **30**, 251–255.

Tsiao, C.J., Carrado, K.A., and Botto, R.E. (1998) Investigation of the microporous structure of clays and pillared clays by ^{129}Xe NMR. *Microporous and Mesoporous Materials*, **21**, 45–51.

Wang, C.M., Baer, D.R., Thomas, L.E., Amonette, J.E., Antony, J., Qiang, Y., and Duscher, G. (2005) Void formation during early stages of passivation: Initial oxidation of iron nanoparticles at room temperature. *Journal of Applied Physics*, **98**, 094308–094307.

Yan, J.M., Zhang, X.B., Han, S., Shioyama, H., and Xu, Q. (2008) Iron-nanoparticle-catalyzed hydrolytic dehydrogenation of ammonia borane for chemical hydrogen storage. *Angewandte Chemie International Edition*, **47**, 2287–2289.

Yuan, P., Yin, X., He, H., Yang, D., Wang, L., and Zhu, J. (2006a) Investigation on the delaminated-pillared structure of TiO_2-PILC synthesized by the $TiCl_4$ hydrolysis method. *Microporous and Mesoporous Materials*, **93**, 240–247.

Yuan, P., He, H., Bergaya, F., Wu, D., Zhou, Q., and Zhu, J. (2006b) Synthesis and characterization of delaminated iron-pillared clay with meso-microporous structure. *Microporous and Mesoporous Materials*, **88**, 8–15.

Yuan, P., Fan, M., Yang, D., He, H., Liu, D., Yuan, A., Zhu, J., and Chen, T. (2009) Montmorillonite-supported magnetite nanoparticles for the removal of hexavalent chromium [Cr(VI)] from aqueous solutions. *Journal of Hazardous Materials*, **166**, 821–829.

Zeng, M., Tang, Y., Mi, J., and Zhong, C. (2009) Improved direct correlation function for density functional theory analysis of pore size distributions. *Journal of Physical Chemistry C*, **113**, 17428–17436.

Zhang, L. and Manthiram, A. (1996) Ambient temperature synthesis of fine metal particles in montmorillonite clay and their magnetic properties. *NanoStructured Materials*, **7**, 437–451.

(*Received 27 September 2010; revised 30 October 2011; Ms. 487; A.E. H. Dong*)